Synthesis and characterization of Ag-delafossites AgBO$_2$ (B: Al, Ga, In) from rapid hydrothermal process

Leon Zwiener[a], Travis Jones[a], Elisabeth Hannah Wolf[a], Frank Girgsdies[a], Milivoj Plodinec[a,b], Alexander Yu. Klyushin [a,c], Elena Willinger[a], Frank Rosowski[d,e], Robert Schlögl[a,f] and Elias Frei*[a]

[a] Dr. L. Zwiener, Dr. T. Jones, E. H. Wolf, Dr. F. Girgsdies, Dr. M. Plodinec, Dr. A. Y. Klyushin, Dr. E. Willinger, Prof. Dr. R. Schlögl, Dr. E. Frei
Department of Inorganic Chemistry, Fritz-Haber-Institut der Max-Planck-Gesellschaft, Faradayweg 4-6, 4195 Berlin, (Germany).
E-mail: efrei@fhi-berlin.mpg.de
[b] Dr. M. Plodinec
Division of Material Physics, Boskovic Institute, Bijenička cesta 54, 10000 Zagreb (Croatia).
[c] Dr. A. Y. Klyushin
Division of Energy Material, Helmholtz-Zentrum Berlin für Materialien und Energie GmbH, Albert-Einstein-Str. 15, 12489 Berlin (Germany).
[d] Dr. F. Rosowski
BasCat – UniCat BASF Joint Lab, Technische Universität Berlin, Hardenbergstraße 36, 10623 Berlin (Germany).
[e] Dr. F. Rosowski, Process Research and Chemical Engineering, Process Catalysis Research
BASF SE, Ludwigshafen (Germany).
[f] Prof. Dr. R. Schlögl, Department of Heterogeneous Reactions, Max-Planck-Institut für Chemische Energiekonversion Stiftstrasse 34 – 36, Mülheim an der Ruhr, 45470 (Germany).

Abstract: A single-step rapid hydrothermal low-temperature process for the formation of high purity polycrystalline Ag-based delafossite oxides 3R-AgBO$_2$ (B: Al, Ga, In) is reported. For the synthesis process reusable and widely available PTFE-lined pressure vessels are used. The presence of an elemental Ag by-phase is traced back to the metastability of the Ag-delafossite under reaction conditions. High purity products are obtained by decreasing the synthesis time requirements by up to 90 %. The effect of the isoelectronic B-site atoms on the structure and bonding situation were comparatively studied experimentally and by ab-initio calculations. Distorted coordination environments are observed in all cases and the nature of the chemical bond changes qualitatively along the series of group 13 B-site atoms Al, Ga and In. This is reflected in systematic changes of the (optical) band gap, the contactless conductivity, the thermal stability and the energetic position of Raman modes which are strongly affected and decrease with increasing atomic number. The establishment of a facile synthesis strategy allows the application of these Ag-delafossite systems in many disciplines, i.e. in heterogeneous catalysis and as optoelectronic device.

Introduction

Delafossite ($CuFeO_2$), first reported in 1873 by C. Friedel, is the name-giving member of a structure type for ternary oxides with the general formula ABO_2.[1] The compositional diversity of the structure includes monovalent *A*-site cations of the semi-noble or noble metals Cu, Ag, Pd or Pt and various trivalent *B*-site cations from group 13, transition metals or lanthanides in the range of $0.53 < r_{IV}^{B(III)} < 1.03$ Å.[2]

The report of p-type conductivity and transparency in $CuAlO_2$ thin films by Kawazoe et al. in 1997 demonstrated the technological importance of this compound class.[3] Since then, Ag-delafossites ($AgBO_2$) containing group 13 (Al, Ga, In) *B*-site cations have been of growing interest due to their optoelectronic properties.[2b, 2c, 4] Hence, their application as transparent conductive oxides (TCO), when deposited as thin films[5] or photocatalysts[6] are explored.

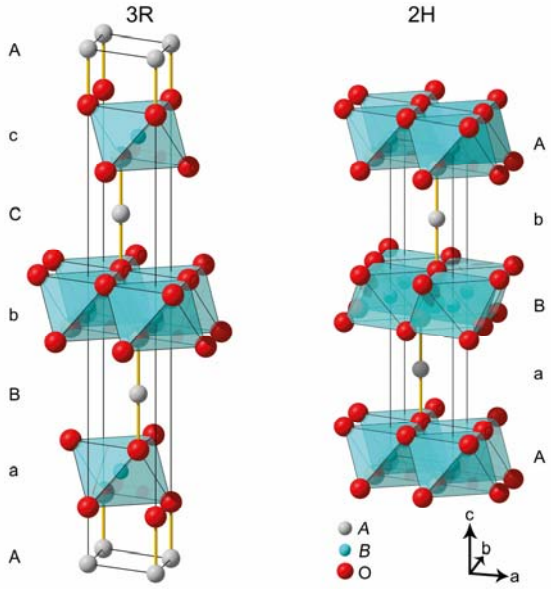

Figure 1: Schematic representation of the ABO_2 delafossite crystal structure for the 3R polytype (left) and 2H (right) polytype.[7] The sequence of the close-packed *A*-layer and BO_2-layer in the direction of the stacking-axis *c* are given.

The crystal structure consists of close-packed Ag^I layers and sheets of slightly distorted edge-shared $B^{III}O_6$ octahedra (BO_2 layer) stacked along the *c*-axis (Figure 1). Linear coordination of Ag^I by two oxygen atoms along the *c*-axis leads to the interlinkage of the adjacent BO_2 layers. Each oxygen atom is tetrahedrally coordinated by four cations (Ag and 3 *B*). Two polytypes of the delafossite structure can form as given in Figure 1.[8] The rhombohedral 3R type (space group *R-3m*, No. 166) originates from the AaBbCc stacking pattern and is experimentally known for all *B*-site ions dealt with in this work.[2a, 9] Besides, the AaBb ordered hexagonal 2H polytype (space group $P6_3/mmc$, No, 194) has been solely obtained for *B*: Al.[10] Because the reagent Ag_2O ($\Delta G_f^0 = -11.2$ kJmol^{-1}[11]) decomposes in open systems already above 573 K[12], the preparation of Ag-delafossites is difficult and requires special conditions. In the early 1970s Shannon et al. introduced different closed-system techniques for their preparation, namely metathetical, oxidizing flux and high temperature hydrothermal methods.[12] However, each method suffered from limitations, such as the formation of highly stable silver halides in case of metathetical reaction

path[12] or Ag_2O/Ag by-phase in the latter cases[2b-d, 5a, 12-13]. Even low amounts of 3R-$AgGaO_2$ could be prepared by solid-state reaction using a diamond anvil cell to generate high pressures (>10^5 bar) and temperatures (≥753 K), as recently reported by Akhtar et al.[14]

Particularly the preparation by hydrothermal synthesis techniques advanced from the early stage of both high-temperature and pressure regimes (773-973 K[9, 12] and up to $20 \cdot 10^3$ bar[9]), utilizing sealed thin-walled Pt or Au tubes to more practical synthesis conditions today. This includes the use of sealed semipermeable fluoro(ethylene-propylene) (FEP) pouches[15] for the preparation of various Ag-delafossites, as introduced by Poeppelmeier and coworkers. The reaction involves equimolar ratios of the corresponding metal oxides and the mineralizer NaOH. 3R-Ag*B*O_2 (*B*: Al, Ga, In) could be obtained at considerable milder temperatures (448-483 K) and autogenous pressures (<20 bar) conditions and reaction times of several days.[2b-d, 6b] In addition, Xiong et al. reported the preparation of 3R-$AgAlO_2$ from the metal nitrates treated under alkaline conditions in a PTFE-lined pressure vessel at 463 K for multiple days. However, the as-prepared product suffered from pronounced Ag_2O contamination which must be leached off by a subsequent multistep washing procedure.[16]

Any potential application of 3R-Ag*B*O_2 (*B*: Al, Ga, In) requires reproducible, scalable and ideally convenient synthetic techniques to obtain products of high purity. We addressed this by developing a time-saving simple hydrothermal synthesis route using common PTFE-lined pressure vessels for 3R-Ag*B*O_2 (*B*: Al, Ga, In). Further, the scalability of the process was demonstrated by the synthesis of 3R-$AgAlO_2$. We comparatively studied the structure and bonding situation in these iso-structural compounds experimentally and by means of ab-initio calculations. As a metal oxidic solid-solution, the ternary silver oxides 3R-Ag*B*O_2 (*B*: Al, Ga, In) presents a potential precursor for Ag/B_2O_3 based catalysts, which were so far realized by impregnation techniques. Consequently, to explore their potential as catalysts, the thermal reactivity of the Ag-delafossites was investigated.

Results and Discussion

Synthesis of Ag-delafossites

3R-$AgAlO_2$

With Ag_2O and α-Al_2O_3 as starting material, the effect of reactant ratio, NaOH (mineralizer) concentration and reaction time on the hydrothermal preparation of 3R-$AgAlO_2$ were investigated using standard PTFE-lined pressure vessels. All samples are designated according to the selected *B*-site ion and the parameter under evaluation (i.e. equimolar Al and Ag ratio is named as Al_1eq). An average particle size of 40 nm for α-Al_2O_3, has been selected based on initial pretests (Table S4). The synthesis parameters for the preparation of 3R-$AgAlO_2$ are listed in Table 1 and the corresponding XRD patterns are presented as close ups in Figure 2 (XRD patterns from 10 – 60° are given in Figure S1 to S3).

Table 1: Experimental details for the preparation of 3R-$AgAlO_2$ by using different reactant ratios, mineralizer concentrations or synthesis times. All samples were prepared at a reaction temperature of 483 K and a fixed batch size of 1.8 g. Data set includes the phase analysis by XRD. Highlighted parameters were varied within a sample series. Optimized conditions shaded (grey).

Sample	Values of parameters			Phases[b]
	Al : Ag[a]	NaOH [M]	t [h]	
Al_1eq	**1 : 1**	0.9	60	3R-$AgAlO_2$, Ag, Ag_2O, Ag_2CO_3
Al_2eq	**2 : 1**	0.9	60	3R-$AgAlO_2$, Ag
Al_3eq	**3 : 1**	0.9	60	3R-$AgAlO_2$, Ag, γ-AlOOH
Al_0.1M	2 : 1	**0.1**	60	3R-$AgAlO_2$, Ag, α-Al_2O_3,γ-AlOOH
Al_0.9M	2 : 1	**0.9**	60	3R-$AgAlO_2$, Ag
Al_1.5M	2 : 1	**1.5**	60	3R-$AgAlO_2$, Ag
Al_60h	2 : 1	0.9	**60**	3R-$AgAlO_2$, Ag
Al_45h	2 : 1	0.9	**45**	3R-$AgAlO_2$, Ag
Al_30h[c]	2 : 1	0.9	**30**	3R-$AgAlO_2$

[a] Molar ratio of elements. [b] The underlined phases are the majority phases (XRD). [c] Graphical representations of the Rietveld refined XRD data given in Figure 7a.

The use of an equimolar ratio of Al and Ag, as selected in the FEP Teflon pouch method[2b, 2c, 6b] leads to the formation of 3R-$AgAlO_2$ and additional by-phases of Ag_2O, Ag_2CO_3 and elemental Ag (Figure 2a). As the molar Al: Ag ratio is raised to 2, Ag remains the sole secondary phase (Figure 2b). A further increase of the Al content to 3 equivalents is not beneficial, as the presence of an additional γ-AlOOH phase is observed. After-reaction analysis of the colorless liquors by ICP-OES noticeable Al amounts were detected in all cases (Table S5).

Hydrothermal synthesis can be regarded as a special type of chemical transport reaction.[17] As such, the dissolution of the educts (hydrolysis of the reactants) is crucial. To enhance the solubility mineralizers[18] such as NaOH are commonly used in the hydrothermal preparation of Ag-delafossites.[2c, 12, 19] The effect of varying the NaOH concentration between 0.1 – 1.5 M on the obtained phase compositions is presented as XRD patterns in Figure 2b. Low mineralizer concentration (0.1M) leads to the presence of undissolved α-Al_2O_3 and the occurrence of γ-AlOOH besides an Ag trace impurity and the crystalline 3R-$AgAlO_2$ main phase. The presence of the aluminous by-product γ-AlOOH is explained by the linkage of the solids Al_2O_3, AlOOH and $Al(OH)_3$ polymorphs as part of the hydration reactions[20]:

$$Al_2O_3\,(s) + H_2O\,(l) \rightleftharpoons 2\,AlOOH\,(s) \qquad (1)$$

$$Al_2O_3\,(s) + 3\,H_2O\,(l) \rightleftharpoons 2\,Al(OH)_3\,(s) \qquad (2)$$

$$AlOOH\,(s) + H_2O\,(l) \rightleftharpoons Al(OH)_3\,(s) \qquad (3)$$

In aqueous solutions, the two polymorphs of Al_2O_3 are not stable below 653 K (Equation 1 + 2), while for $Al(OH)_3$ they are not stable above 353 K (Equation 2 + 3). They transform into the kinetically favored γ-modification of AlOOH (Eq. 1 + 3)[21], which is the solubility-controlling phase under hydrothermal conditions.[22] Its solubility has been extensively studied and increases at elevated temperature and strong alkaline media.[22-23] Hence, no aluminous secondary phases were present after the NaOH concentration was adjusted to ≥ 0.9 M, but almost exclusively 3R-$AgAlO_2$ (Figure 2b, Al_0.9M and Al_1.5M). Besides, the as-prepared samples still featured trace impurities of Ag (<1 wt. %). Its presence has already been frequently reported in the context of Ag-delafossite synthesis.[2b, 24] and identified as impurity on the Ag_2O educt.[2d] However, in the present work this obstacle was not observed after a significant decrease of the hydrothermal reaction time from the common 60 h to 30 h. As evidenced by the given XRD data in Figure 2c phase pure 3R-$AgAlO_2$ was obtained (see also Table 1).

A possible explanation for the presence of the Ag by-phase might be the limited stability of the delafossite product phase under the hydrothermal reaction conditions. To clarify this issue, the stability of the phase-pure 3R-$AgAlO_2$ and the educt Ag_2O were investigated in a model experiment by exposing them to identical hydrothermal reaction conditions. The corresponding XRD patterns of the treated samples are presented as close ups in Figure 3a. In the case of the ex_Ag_2O sample the diffraction pattern still coincides solely with the pure Ag_2O (PDF2 card no 41-1104). After the 60-hour hydrothermal treatment at 483 K 3R-$AgAlO_2$ (ex_$AgAlO_2$, Figure 3a) decomposed to Ag_2O and elemental Ag. The latter is evidenced by the presence of the Ag 111 reflection at 38.1° 2θ (diffraction pattern from 25 - 75 ° 2θ in Figure S4). This observation further corroborated the metastability of the Ag-delafossite phase under the given synthesis conditions.

In order to further investigate the influence on the actual synthesis of 3R-$AgAlO_2$, the hydrothermal synthesis time was systematically varied in the range of 3 – 60 h in the subsequent experiments. To fasten the dissolution of the educts, increase their liquid-phase transport and intensify the heat transfer the reaction mixture was stirred. For all samples, quantitative phase analysis of the multicomponent mixtures using X-ray powder diffraction data has been performed using the Rietveld method. The evolution of the approximate phase amounts as a function of the synthesis time are presented in Figure 3b. The corresponding diffraction patterns are given in Figure S5. Already after 3 h the presence of about 10 wt. % 3R-$AgAlO_2$ is detected. After a further increase to 10 h its proportion has increased to 95 wt. %. The contribution of the α-Al_2O_3 educt drastically decreased, respectively both crystalline Ag_2O and Ag_2CO_3 are no longer detectable. As highlighted, high purity 3R-$AgAlO_2$ could be obtained in the time frame of 12 – 19 h. An additional increase of the hydrothermal synthesis time (40 – 60 h) is not beneficial. This is due to the rising contribution of a Ag by-phase leading to a contamination of about 12 wt. % Ag after 60 h.

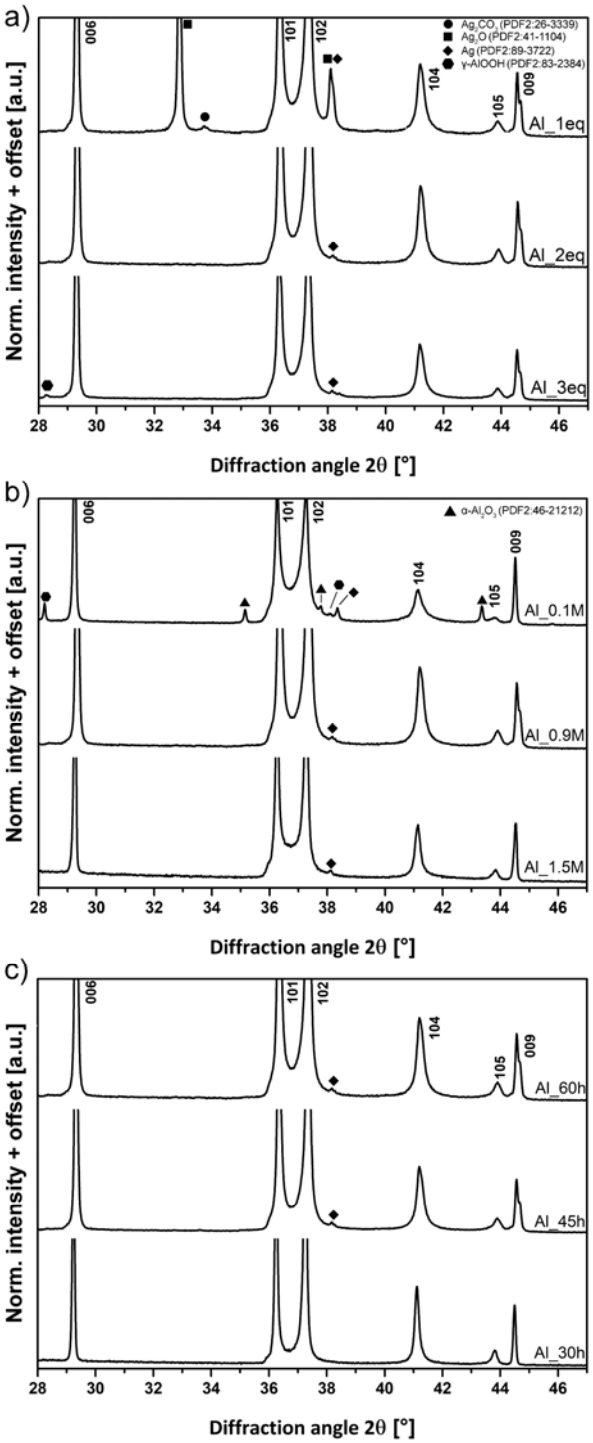

Figure 2: XRD patterns of as-synthesized samples obtained after variation of educt ratio (a), NaOH content (b) and reaction time (c). Indices are given for the crystalline main phase 3R-AgAlO2. The corresponding overview XRD patterns from 10 – 60° 2θ are given in Figure S1 - S3.

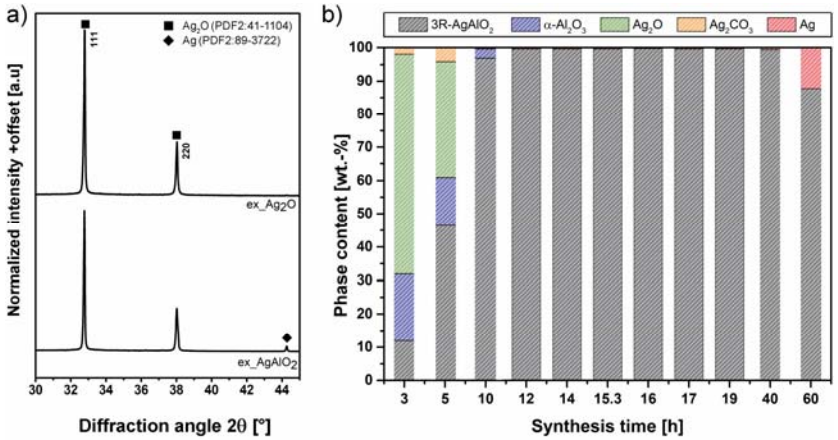

Figure 3: XRD patterns of Ag_2O and 3R-$AgAlO_2$ after treatment in 0.9 M NaOH at 483 K for 60 h (a) and the evolution of the phase composition as a function of the applied hydrothermal synthesis time (b). Phase contents derived by quantitative XRD analysis. Optimized synthesis time frame highlighted (12-19 h).

The volcano-shaped time dependent evolution of the 3R-$AgAlO_2$ phase contribution (Figure 3b) evidently indicates the presence of competing processes taking place during the hydrothermal treatment. The sketch in Figure 4 visualize a proposed reaction scheme, whereby a detailed kinetic analysis of these processes is beyond the scope of this work. However, it is expected that this includes at least the Ag-delafossite phase formation and its concurrent decomposition attributed to its apparently metastable nature (see sketch in Figure 4). Hence, phase-pure 3R-$AgAlO_2$ may by all means solely be obtained as the kinetically favored product. The solid decomposition products detected by XRD (Figure 3a) are Ag_2O and elemental Ag, of which the former apparently readily reacts again to the Ag-delafossite phase. The major soluble species of the amphoteric Ag_2O[25] is reportedly $[Ag(OH)_2]^-$ [26]. In contrast, the elemental Ag features a lower solubility in alkaline media[26] and presumably accumulates in the reaction mixture over time and is detected in the as-prepared product by XRD analysis (60 h in Figure 2c or Figure 3b). By agitation these processes are accelerated, however this also makes shorter reaction times feasible. In a first scale-up, high-purity product in the double-digit gram range was obtained (Figure S6).

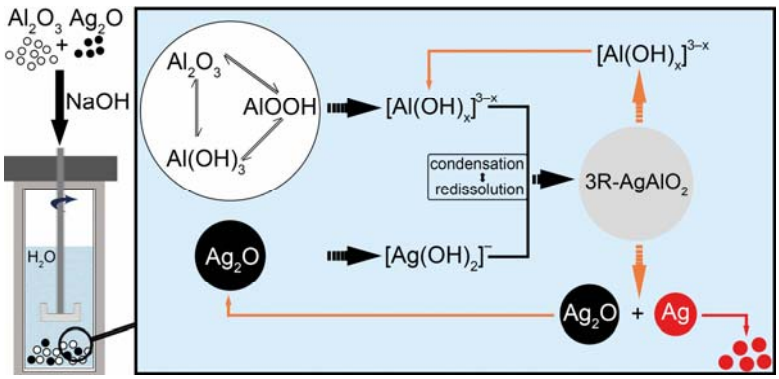

Figure 4: Sketch of the proposed reaction scheme for the 3R-$AgAlO_2$ phase formation and decomposition (orange arrows) via hydrothermal treatment. Of the specified compounds, only the solid phases are detected in the course of this work (XRD).

3R-AgGaO$_2$

For the Ag-delafossite comprising the heavier group 13 element Ga as *B*-site ion, the optimized synthesis of 3R-AgAlO$_2$ served as the starting point. The aqueous chemistry of Ga^{III} and Al^{III} share some resemblance, including the amphoteric behavior of their oxides.[18] 3R-AgGaO$_2$ was prepared by the hydrothermal reaction of the respective metal oxides in 0.9 M NaOH solution at 483 K. In addition, the effect of reactant ratio and the synthesis time have been examined to obtain a high-purity product. The experimental details are summarized in Table 2 and the corresponding powder X-ray diffraction patterns are presented in Figure 5 (overview patterns in Figure S7 and S8).

The use of stochiometric amounts of the amphoteric Ga-sesquioxide (Ga$_2$O$_3$) and Ag$_2$O lead to the formation of 3R-AgGaO$_2$ and additional minor contributions from Ag-containing byproducts namely Ag$_2$O, Ag$_2$CO$_3$ and Ag (Figure 4a). Adjusting the Ga content to a value ≥2 eq., 3R-AgGaO$_2$ formed almost exclusively.

Table 2 Experimental details of the prepared 3R-AgGaO$_2$ samples by varying reactant ratios or reaction times. Batch size (1.8 g), NaOH concentration (0.9 M) and reaction temperature (483 K) fixed for all experiments. Data set includes the phase composition (XRD). Final set of optimized parameters shaded (grey).

Sample	Values of parameters		Phases[b]
	Ga : Ag[a]	t [h]	
Ga_1eq	**1 : 1**	30	3R-AgGaO$_2$, Ag, Ag$_2$O, Ag$_2$CO$_3$
Ga_2eq	**2 : 1**	30	3R-AgGaO$_2$, Ag
Ga_3eq	**3 : 1**	30	3R-AgGaO$_2$, Ag
Ga_30h	2 : 1	**30**	3R-AgGaO$_2$, Ag
Ga_20h	2 : 1	**20**	3R-AgGaO$_2$, Ag
Ga_10h[c]	2 : 1	**10**	3R-AgGaO$_2$, (Ag)

[a] Molar ratio of elements. [b] The underlined phases are the majority phases (XRD). [c] Graphical representations of the Rietveld refined XRD data given in Figure 7b.

Besides, the as-prepared sample contained minor elemental Ag contamination (<1 wt. %). Overall, the results are similar to the *B*-site ion Al (see Figure 2a). However, here no crystalline *B*-containing phase was observed after an additional increase of the reactant ratio (Ga_3eq, Figure 5a). This might be correlated to the less pronounced amphoteric character of Ga oxides, which comprise some acidic properties. This goes in line with the reported higher solubility of Ga^{III} (compared to Al^{III}) in alkaline media at elevated temperature (473 K).[27]

As in the Al-case, the presence of the Ag by-phase was further addressed by a decrease in the reaction time. By lowering the hydrothermal synthesis time from 30 h to 10 h, the contribution of the Ag by-phase could be largely reduced, close to the detection limit (Ga_10h, Figure 5b.). This observation was tentatively interpreted as being related to the metastability of the isomorphous

Ag-delafossite product phase. As a side effect, the total synthesis time requirement was successfully cut by 90 %, when compared to the established FEP pouch method.[4b]

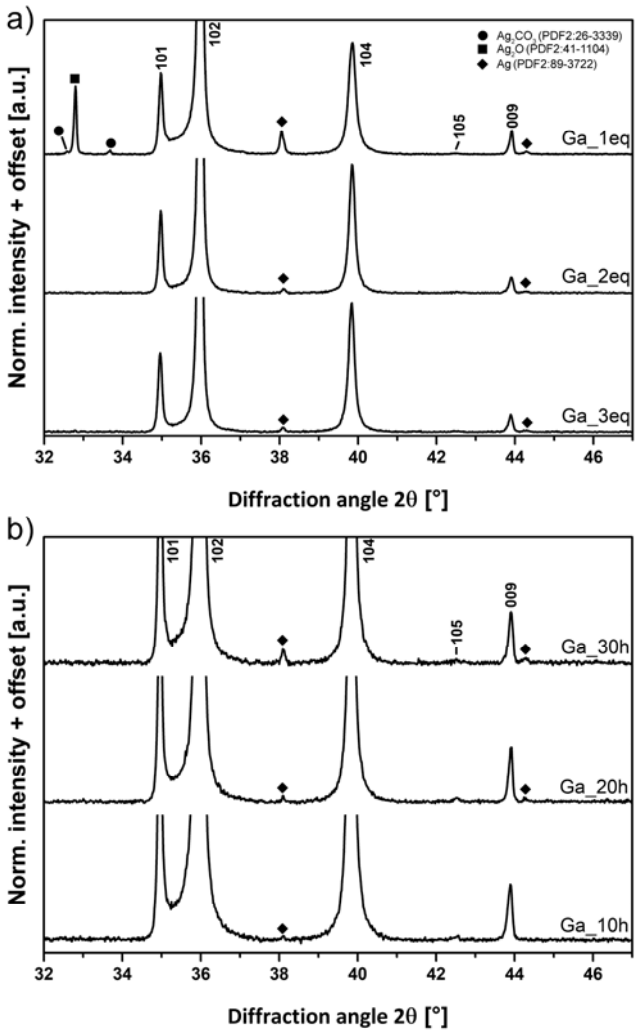

Figure 5: XRD patterns of as-synthesized samples obtained after variation of educt ratio (a) and reaction time (b). Indices are given for the crystalline main phase 3R-$AgGaO_2$.The corresponding overview diffraction patterns from 10 – 60° 2θ are given in Figure S7 and S8.

3R-$AgInO_2$

The experimental parameters for the hydrothermal synthesis of the Ag-delafossite comprising the group 13 *B*-site ion In, are given in Table 3. Within the investigated educt ratios, the formation of 3R-$AgInO_2$ as the crystalline mainphase could be observed (Figure 6). However, the as-prepared samples suffered from the presence of In-containing secondary phases, namely the sesquioxide educt (In_2O_3) and $In(OH)_3$. This might be attributed to the fairly limited solubility of In oxides in alkaline media (in contrast to amphoteric Al^{III} and Ga^{III}).[28] Hence, a reduction of the hydrothermal synthesis time did not seem reasonable, as it was expected to lead to a rising contribution of the In-containing by-phases in the final product. Therefore, the reactant ratio was fixed to one and the

batch size was decreased (1.4 g). As a result, no $In(OH)_3$ contamination could be detected in the product anymore, but a trace impurity of elemental Ag (Figure 7c). As for the lighter group 13 *B*-site ions Al and Ga, its presence is interpreted as an indication for the metastability of the Ag-delafossite product phase.

Table 3 Experimental details of the prepared 3R-$AgInO_2$ samples by varying reactant ratios and sample mass. For all experiments the same NaOH concentration (0.9 M), reaction temperature (483 K) and reaction time (30 h) were used. Data set includes the phase composition (XRD). Final set of optimized parameters shaded (grey).

Sample	Values of parameters		Phases[b]
	In : Ag[a]	Batch size [g]	
In_1eq	**1 : 1**	1.8	<u>3R-$AgInO_2$</u>, $In(OH)_3$, In_2O_3
In_1.5eq	**1.5 : 1.0**	1.8	<u>3R-$AgInO_2$</u>, $In(OH)_3$, In_2O_3
In_2eq	**2 : 1**	1.8	<u>3R-$AgInO_2$</u>, $In(OH)_3$, In_2O_3
In_1.4g[c]	1 : 1	**1.4**	<u>3R-$AgInO_2$</u>, In_2O_3, Ag

[a] Molar ratio of elements. [b] The underlined phases are the majority phases (XRD). [c] Graphical representations of the Rietveld refined XRD data given in Figure 7c.

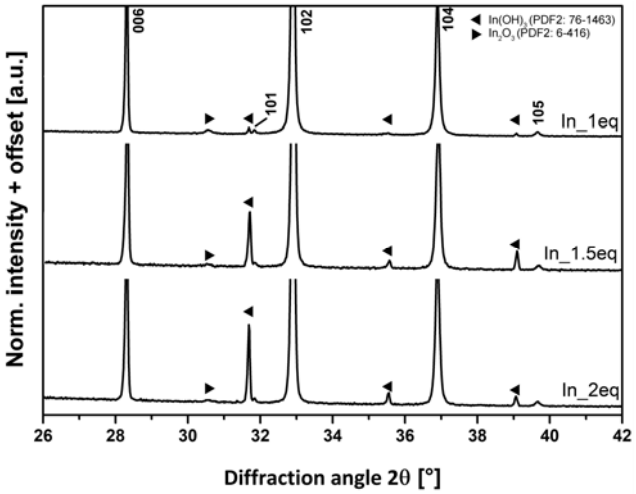

Figure 6: XRD patterns of as-synthesized samples obtained after variation of educt ratio. Indices are given for the crystalline main phase 3R-$AgInO_2$.The corresponding overview diffractograms from 10 – 60° 2θ are given in Figure S9.

The three isostructural ternary oxides 3R Ag*B*O_2 (*B*: Al, Ga, In) obtained by the optimized synthesis protocols (see shaded rows in Table 1-3) were further comparatively studied with respect to their structure and bonding situation.

Structural properties of 3R-Ag*B*O_2

Table 4: Overview of selected 3R-$AgBO_2$ (B: Al, Ga, In) samples including their metal ratios (XRF, ICP-OES), specific surface areas determined by N_2-physisorption (SA_{BET}), band gap energies (E_{gap}), conductivity, Raman active modes and decomposition temperatures ($T_{decomp.}$, STA-EGA) as well as mass losses due to decomposition (TG). For comparison, the calculated values are given in brackets. In the case of the E_{gap} the calculated values using LDA, PBE and SCAN are given.

Sample	Metal ratio [Ag]/[*B*]		SA_{BET}	E_{gap}	Conductivity [$mScm^{-1}$]		Raman modes [cm^{-1}]		$T_{decomp.}$	Mass loss
	EDX	ICP-OES	[m^2g^{-1}]	[eV]	303 K	473 K	E_g	A_{1g}	[K]	[wt.%][b]
3R-$AgAlO_2$	1.07 ± 0.06	-[a]	1.5	3.2 (1.5; 1.3; 2.1)	0,05	0,22	406 (411)	711 (714)	1075	4.5 (4.8)
3R-$AgGaO_2$	1.08 ± 0.03	1.06	2.1	2.5 (0.5; 0.6; 1.0)	0,19	0,37	378 (302)	674 (652)	960	3.8 (3.8)
3R-$AgInO_2$	0.98 ± 0.15	1.04	1.8	2.1 (0.2; 0.2; .0.7)	1,1	2,7	342 (344)	614 (618)	900	3.1 (3.1)

[a]: No data given, as only partial dissolution of the compound. [b]: Average value of three measurements.

The obtained ternary oxides of the general formula Ag*B*O_2 (*B*: Al, Ga, In) all crystallize in the delafossite structure. As such, the effect of the *B*-site cation on the structural parameters and the nature of the chemical bonding were investigated. In the delafossite structure nominally Ag^{I} (*A*-site) and the group 13 cations Al^{III}, Ga^{III} or In^{III} (*B*-site) are present. The anisotropic delafossite structure features single *B*O_2 layers of close-packed *B*O_6 octahedra stacked along the *c*-axis and linked to one another by linear coordination of Ag with two oxygen atoms. For oxygen a tetrahedral coordination results with one Ag and three *B*-site cations (see Figure 1). All atoms are located on special positions. The crystal structure is described by three variables, the lattice parameters *a* and *c* and the *z*-position of the oxygen atom.[9] Rietveld refinement of these parameters started from the experimentally available single-crystal structure data of 3R-$AgInO_2$ (ICSD entry 202429)[9], which also served as a starting point for both remaining isostructural Ag-delafossites with *B*: Al, Ga.

Rietveld refinement of the XRD patterns confirms phase-purity for the 3R-$AgAlO_2$ sample (Al_30h, Figure 7a). In case of 3R-$AgGaO_2$ (Ga_10h), a very small peak which corresponds to the Ag (111) diffraction, is present at $2\theta \approx 38.1°$ (Figure 7b, inset). The diffraction pattern of 3R-$AgInO_2$ (In_1.4g) shows the contribution of an additional In_2O_3 (ICSD entry 190344) trace impurity (Figure 6c, inset). While the presence of these additional phases is clearly detectable by PXRD, a reliable quantitative analysis of such traces, which can be estimated to be well below 1 wt. %, is beyond the possibilities of our Rietveld analysis. This is in excellent agreement with the determined cationic content of the samples close to stoichiometry (Table 4). To simplify matters, in the following all samples are named after their respective delafossite phase (i.e. Al_30h as 3R-$AgAlO_2$).

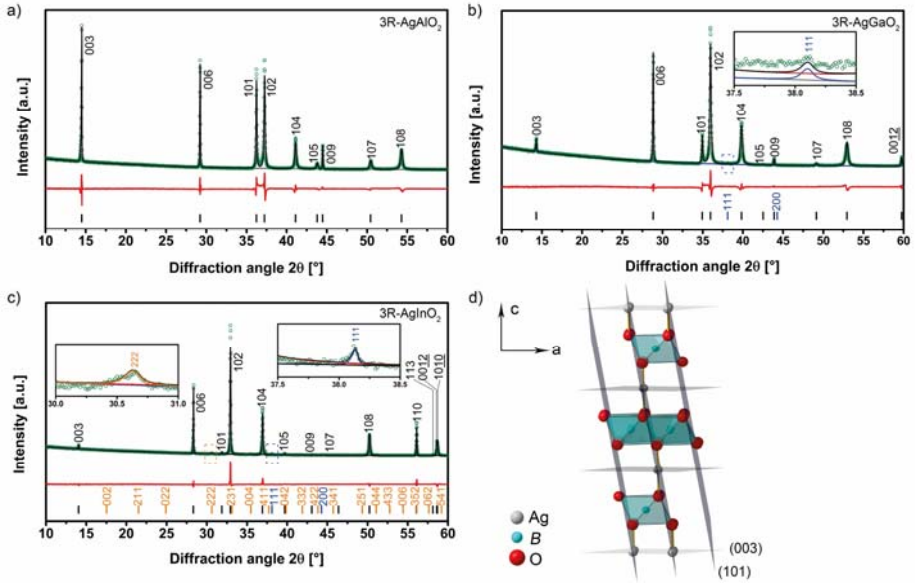

Figure 7: Graphical representations of the Rietveld refined Ag-delafossite powder XRD data (a-c) and delafossite unit cell of 3R polytype with (003) and (101) viewed along *b*-axis (d). Experimental pattern (green circles), calculated data (black line), separate phase contributions of delafossite phase (red line), Ag (blue line) and In_2O_3 (orange line), background (grey line), difference curve (red curve) and peak positions (ticks) are given. Insets in b) and c) show contribution of Ag (blue ticks) and In_2O_3 (orange ticks) to the diffraction patterns.

The observed X-ray diffraction patterns reflect the anisotropy of the delafossite crystal structure. All samples exhibit a varying degree of anisotropic peak broadening, with sharper interlayer *00l* and intralayer *hk*0 reflections and broader mixed *hkl* reflections. The effect is strongest for 3R-$AgAlO_2$ and least pronounced in 3R-$AgInO_2$. The same trend is observed for the asymmetry of the bases of the 101 and 102 reflections, which leaves a visible signature in the residual of the Rietveld fits shown in Figure 7. We suspect that these effects are caused by 2H-type stacking faults within the 3R polytype matrix, which would leave the coherency of diffraction and homogeneity of *d*-spacings mostly undisturbed along the stacking axis *c* and within the *a*,*b* plane (Figure 7d), respectively, while affecting mainly the diagonal directions. This idea is supported by the fact that the synthesis of the pure 2H phase has been reported only for the Al compound[10]. Furthermore, both polytypes of the Ag-delafossite $AgAlO_2$, 2H and 3R have about the same total energies[4g]. We assume that the 2H variant becomes less favorable compared to the 3R structure for the heavier *B* cations, thus resulting in a lower faulting probability.

The layered structure was further investigated by TEM analysis. High-resolution STEM images with Z-contrast visualize the layered delafossite structure of 3R-Ag*B*O_2 (*B*. Al, Ga, In), as presented in Figure 8a-c. With higher atomic number of the group 13 *B*-site cation, the measured interplanar distances of d(003) planes (spacing of two adjacent Ag layers along the *c*-axis, Figure 7d) becomes larger. The measured values are in good agreement with the XRD data (*B*; Al: 6.1 Å, Ga: 6.2 Å, In: 6.3 Å). Morphological analysis of the samples was performed by SEM. The SEM micrographs are given in Figure 8d-f. The presence of partially intergrown hexagonal shaped platelets in the micrometer range is observed for all samples. Besides, the occurrence of holes in a minor fraction of the plates leading to a doughnut-like shape was solely found for 3R-$AgAlO_2$ featuring edge lengths of up to 2.5 µm and a maximum thickness of 0.5 µm. Textural properties of the faceted particles drastically varied from smooth to rough. Overall, the 3R-$AgGaO_2$

sample consists of smaller and thicker platelets (up to 1 µm edge length) and less well-defined sub µm-sized particles. Even thicker platelets (0.8 µm) are obtained when the heavier group 13 element In is present as the *B*-site cation as given in 3R-$AgInO_2$. The specific BET surface area varies at a low level around 2 m^2g^{-1} for all samples (Table 4). phase.

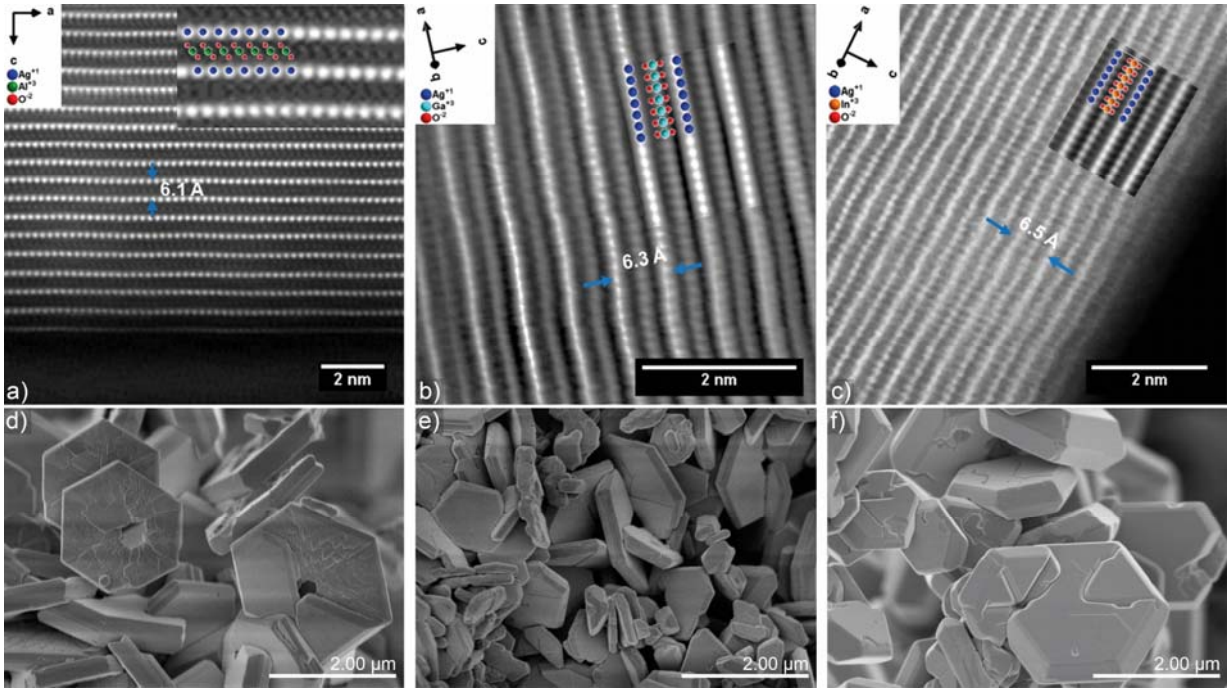

Figure 8*:* Atomic resolution HAADF images of the layered crystalline delafossite structures with inserted schematic models and Fourier filtered images for: a) 3R-$AgAlO_2$ along the [010] zone axis, b) 3R-$AgGaO_2$ along the [120] zone axis and c) 3R-$AgInO_2$ along the [120] zone axis. SEM images of 3R-$AgAlO_2$ (d), 3R-$AgGaO_2$ (e) and 3R-$AgInO_2$ (f). The blue arrows indicate the interplanar distance between (003) planes. The corresponding STEM-ABF images are presented in Figure S10.

For all Ag-delafossite compounds in this work, a distortion of the octahedral coordination geometry of the *B*-site ion is observed. To some extent, the BO_6 octahedra are flattened along the *c*-axis. This observation is given in Figure 9b as the ratio of intralayer (in the *ab*-plane) and interlayer O-O distances implying a similar degree of distortion for all samples. The O*B*O-angle deviates from the ideal octahedral angle of 90°. The experimental determined deviation is in the range of 7.0° (Table 5), however no systematic trend for the 3R-AgBO_2 samples can be deduced, since all values lie well within 3ESD (0.5°). Consequently, a similar deformation is observed for the OAgB_3 tetrahedral moieties (Figure 12c). It may be noted that the slope of the *B*-O distances over the corresponding *B* radii red line in Figure 9a) is almost exactly 1, which means that the simple “hard sphere” model works very well for the *B*-O interaction, in contrast to the Ag-O bonding.

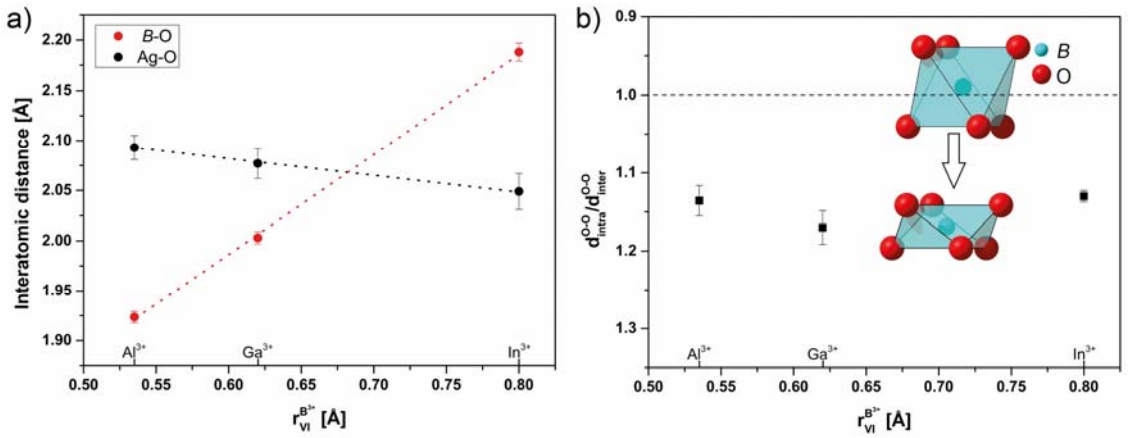

Figure 9: Trend of interatomic distances B-O and Ag-O (a) and the deformation of the BO_6 octahedra (b) as a function of the 6-coordinate Shannon B^{3+} radii (r_{VI}^{B3+}). Error bars of 3ESD (estimated standard deviations) are given for interatomic distances. A ratio for the intralayer O-O distance (d_{intra}^{O-O}) and interlayer O-O distance (d_{inter}^{O-O}) greater than one reveals flattening of the BO_6 octahedra along the c-axis as schematically shown.

According to the PDOS analysis, as expected, the formally empty *B* states (s^0 p^0) mainly contribute to the conduction band, which hybridize with the O-p and Ag-d states (Figure 10). The position of the conduction band is steered by the selected group 13 *B*-site atom. Going from *B*: Al to In, increasing contribution of the s states on the lower energy side of the conduction band appear (olive green curves in Figure 10). This leads to a stepwise decrease in the calculated energetic gap between valence band and conduction band and an increase in covalent character with increasing size (respectively softness) of the *B*-site atom.

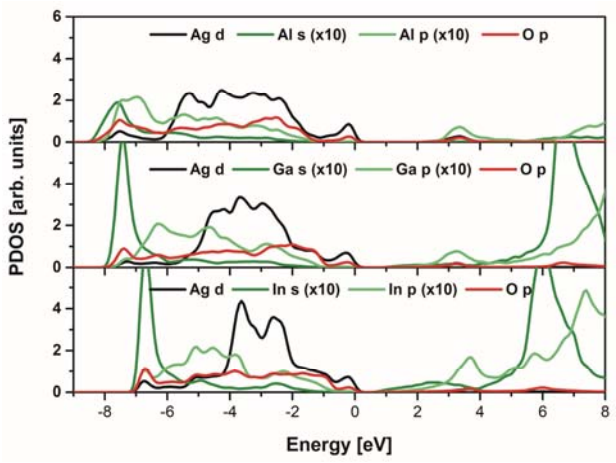

Figure 10: The projected density of states for 3R-$AgAlO_2$ (top panel), 3R-$AgGaO_2$ (middle panel) and 3R-$AgInO_2$ (bottom panel) obtained using the SCAN functional.

Table 5: Rietveld refined and ab-initio calculated lattice parameters, z-position of oxygen, selected interatomic distances and angular deviation of BO_6 in 3R-$AgBO_2$ (B: Al, Ga, In) along with experimental results from Ref. [9, 12]. In addition, the effective ionic Shannon radii are given for the B-site ions featuring a coordination number of six. In addition, the ionic radius of Ag_{II}^{+} is 0.67 Å and O_{IV}^{2-}: 1.35 Å[2e]. For the 3R-$AgBO_2$ polytype, the atomic fractional coordinates are Ag (3a) (0, 0, 0), B (3b) (0, 0, 0.5) and O (6c) (0 ,0, z). Lattice constant a is equal to d(Ag-Ag) [Å].

Sample	*a* [Å]	*c* [Å]	z(O)/*c*	d(Ag-O) [Å]	d(*B*-O) [Å]	Δ(O-*B*-O) [°][a]	r_{VI}^{B3+}[Å] [2e]
3R-$AgAlO_2$							0.535
Rietveld refined	2.8870(2)	18.3161(3)	0.1143(2)	2.093(4)	1.9236(19)	7.25(13)	
Ref. [12]	2.890(2)	18.27(2)					
Calculated							
LDA	2.84	18.32	0.11559	2.11	1.89	7.58	
PBE	2.92	18.81	0.11588	2.18	1.94	7.86	
SCAN	2.88	18.32	0.11462	2.10	1.95	7.35	
3R-$AgGaO_2$							0.620
Rietveld refined	2.9909(2)	18.5548(4)	0.1120(2)	2.077(5)	2.003(2)	6.59(15)	
Ref. [12]	2.9889(2)	18.534(2)					
Calculated							
LDA	2.98	18.63	0.11286	2.10	1.99	6.92	
PBE	3.03	18.79	0.11280	2.12	2.02	7.16	
SCAN	2.98	18.58	0.11276	2.10	1.99	6.91	
3R-$AgInO_2$							0.800
Rietveld refined	3.2768(2)	18.8865(2)	0.1085(3)	2.049(6)	2.188(3)	6.99(17)	
Ref. [9]	3.2768(7)	18.8779(70)	0.1100(4)	2.0766(76)	2.1734(37)	7.851(164)	
Calculated							
LDA	3.26	18.92	0.11018	2.08	2.16	7.74	
PBE	3.34	19.11	0.11000	2.10	2.21	8.07	
SCAN	3.27	18.91	0.10973	2.08	2.17	6.63	

[a] Angular deviation from the ideal octahedral angle of 90°.

This trend is also reflected in the experimentally determined optical band gaps of the ternary silver oxides (3.2 eV (B: Al), 2.5 eV (Ga) to 2.1 eV (In)). The band gaps are derived on the basis of Tauc plots, calculated from the measured diffuse reflectance spectra of 3R-Ag*B*O_2 (*B*: Al, Ga, In) and given in Figure S12 and Table 4. The as-prepared powdered samples are of white (3R-$AgAlO_2$), olive green (3R-$AgGaO_2$) and orange (3R-$AgInO_2$) color. The experimental values are in qualitative agreement with the calculated values (Table 4). Furthermore, the conductivity of the samples was measured using the contact free Microwave Cavity Perturbation Technique (MCPT). In line with the decreasing band gaps, the conductivity increases within the series of 3R-Ag*B*O_2 (*B*: Al, Ga, In) samples for larger *B*-site cations (Figure S12). Besides, as expected for semiconducting samples, the conductivity increases to higher temperatures (Table 4, 303 vs. 473 K).

To further study the effect of the *B*-site cation on the local environment, Raman spectroscopy was performed on the 3R-Ag*B*O_2 (*B*: Al, Ga, In) samples. Factor group analysis was performed on the 3R-delafossite structure (space group *R-3m*, No. 166) using the symmetry adapted modes (SAM) application of the Bilbao crystallographic server [29]. The primitive unit cell has four atoms, which gives rise to 12 normal modes. Accordingly, the total irreducible representation at the Brillouin zone center excluding both acoustic modes ($\Gamma_{acoustic} = A_{2u} + E_u$) gives two Raman active phonon modes ($\Gamma_{Raman} = A_{1g} + E_g$) and four IR active phonon modes ($\Gamma_{IR}=2A_{2u} + 2E_u$). The A modes describe the movement along the *c*-axis, while E modes do in the perpendicular direction in the *ab*-plane (Figure 11b). The measured Raman spectra are given in Figure 11a. The spectrum of 3R-$AgAlO_2$ (top trace) features two distinct bands at 711 cm^{-1} (calc. 714 cm^{-1}) and 406 cm^{-1} (calc. 411 cm^{-1}), which agrees well with the calculated Raman mode positions.

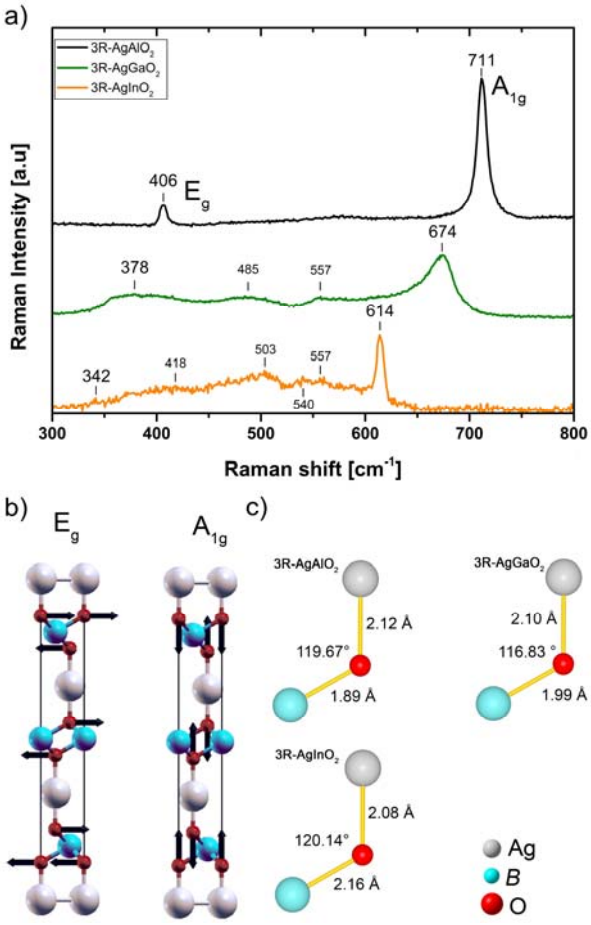

Figure 11: Raman spectra (a), corresponding displacement patterns (b) and calculated bond lengths and angles of the local environment of oxygen (c) for 3R-Ag*B*O_2 (*B*: Al, Ga, In).

The former could be assigned to the A_{1g} mode, which is associated to oxygen vibration along the hexagonal c-axis, in the direction of the Ag-O bond. The latter at 406 cm^{-1} is assigned to the double degenerate E_g mode in the ab-plane (Figure 11b). Note that only oxygen contributes to both Raman active mode, since Ag and the group 13 element are stationary. Oxygen is in a distorted tetrahedral coordination with one Ag^{I} and three B^{III} (Figure 11c). The position of these bands is sensitive to the nature of the B-site ions. The intense A_{1g} mode shifts progressively to lower

wavenumbers for 3R-$AgGaO_2$ (674 cm^{-1}, calc. 652 cm^{-1}) and 3R-$AgInO_2$ (614 cm^{-1}, calc. 618 cm^{-1}). A similar gradual shift is observed for the lower wavenumber bending E_g mode that is located at 378 cm^{-1} for 3R-$AgGaO_2$ (calc. 302 cm^{-1}) and 342 cm^{1} for 3R-$AgInO_2$ (calc. 344 cm^{-1}). As the Ag-O distance remains almost constant in all samples (2.10 ± 0.02 Å, Figure 11c), this indicates the frequency depends strongly on the nature of the B-O bonding.

The delafossite Raman spectra should only feature two modes. However, for *B*: Ga and In they deviate from the number of modes predicted by group theory and feature additional broad signals around 400 – 560 cm^{-1} located between E_g and A_{1g}. These weak modes become more apparent and complex along the series of samples. Their presence cannot be assigned to the trace impurities (Figure 7). Besides, they have been previously reported in the case of *B*: Ga (485 cm^{-1} and 557 cm^{-1})[14, 30] and similar observations have been made for Cu-delafossites (*B*: Al, Cr, Fe, Ga)[31]. To the best of the authors knowledge, no Raman measurements of 3R-$AgInO_2$ have been reported, so far. These low-intensity bands might originate from the distortion of the oxygen moieties or present defects (oxygen non-stoichiometry) as Raman spectroscopy is sensitive to the crystal symmetry and changes of the local structure.

Thermal reactivity of 3R-Ag*B*O_2

In order to evaluate the suitability of these materials as heterogeneous catalyst precursors, the thermal behavior of all samples was investigated by STA/EGA techniques in Ar up to 1273 K. The results are presented comparatively in the different panels of Figure 12. The individual patterns are given in Figure S14. Upon thermal treatment of 3R-$AgAlO_2$ the release of H_2O (m/z 18, up to about 600 K) is detected by EGA which is attributed to its desorption from the surface. The minor release of CO_2 (m/z 44, up to 750 K) might be correlated to the decomposition of incorporated carbonate species in the delafossite structure (Figure 12c). The ongoing temperature increase leads to the renewed release of H_2O, present as a broad signal centered around 906 K. Its occurrence is attributed to the dehydration of hydroxyl group condensation from the hydroxylated metal oxide surfaces[32]. As the samples were prepared under hydrothermal synthesis conditions and not calcined prior to the STA. These processes account for a limited mass loss of about 0.2 % (average of 3 measurements). Similar observations are made for *B*: Ga (0.4 %, Figure S14b) and In (0.1 %, Figure S14c) as well. The ternary oxides decompose in a single endothermal (Figure 12b) main event, according to the given reaction:

$$4\ AgBO_{2(s)}\ (B\text{: Al, Ga, In}) \rightarrow 4\ Ag_{(s)} + 2\ B_2O_{3(s)} + O_{2(g)}\uparrow \qquad (1)$$

This event is located at 1075 K for the 3R-$AgAlO_2$ and coincides with a mass loss of 4.5 % (due to oxygen release) which is close to the calculated value (4.8 wt. %). In the case of 3R-$AgGaO_2$ the decomposition is shifted to 960 K, respectively 900 K for 3R-$AgInO_2$ (Figure 12a). In both cases, the detected mass losses are in excellent agreement with the theoretic values (Table 4). Investigations for the verification of the proposed non-stoichiometry of the anion lattice were performed by temperature programmed oxidation experiments (TPO) in 0.25 % O_2/He. Despite the use of up to 1.5 g 3R-Ag*B*O_2, no oxygen uptake could be observed from 298 K up to below the decomposition temperature (details see SI, Figure S16). The presence of elemental Ag and

the respective *B*-site metal(III) oxide is verified for all samples after the STA by XRD analysis (Figure S14). In addition the endothermal DSC event detectable for all samples around 1239 K indicates the melting of Ag[33].

According to Kandpal et al. the structural stability of the ternary oxides originates from the strong ionic character of the *B*-O bonding interaction.[4h] Thus, the observed trend towards lower decomposition temperatures along the series of group 13 *B*-site atoms is in line with the expected lower attractive ionic *B*-O interaction when going from the hard Al to the softer In. Further, the thermal reactivity results of the 3R-AgBO_2 series show the potential temperature and application range of these materials as precursors, supports or catalysts under oxidizing conditions. The detailed investigation as catalytic material is beyond the scope of this manuscript.

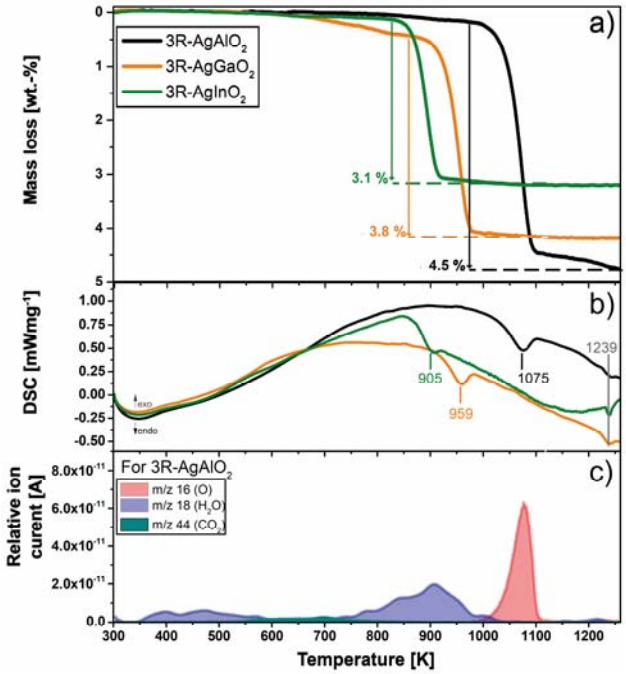

Figure 12: Simultaneous thermal analysis (STA) of 3R-AgBO_2 (*B*: Al, Ga, In) by TG (a), DSC (b) and EGA (c) in Ar atmosphere. For the sake of clarity, only the MS data (relative ion currents) for *B*: Al is given in panel c.

Conclusions

We herein report on the improved synthesis of 3R-AgBO_2 (*B*: Al, Ga, In). The frequently reported presence of an elemental Ag by-phase originates from the metastability of the delafossite phase under reaction conditions. Hence, the ternary Ag oxides represent the kinetically favored product making shorter hydrothermal synthesis times necessary. By optimizing the reaction parameters, the synthesis time requirements were successfully reduced by up to 90 %, obtaining high-purity products. By the selection of isoelectronic group 13 ions as *B*-site atoms, the structure and bonding situation were comparatively studied experimentally and by means of ab-inito calculations. Heavier *B*-site atoms lead to a pronounced unit cell expansion, reflected in longer *B*-O bonds and overall distorted coordination environments. In contrast, the Ag-O distance remains

largely unchanged by the substitution. The nature of the *B*-O bonding interaction changes qualitatively along the group 13 atoms Al, Ga and In as indicated by the analysis of the electronic structure and supported by experimental evidences. Properties such as the (optical) band gap, contactless conductivity, energetic position of Raman modes and the thermal stability are strongly affected and decrease with increasing atom number/softness of the B-site atom. Besides, the variation of the B-site cation offers the possibility to adjust the material properties, potentially applied as catalytic material for oxidation reactions (precursor, support, catalyst) and optoelectronic devices.

Experimental Section

General: All reagents were purchased from commercial vendors and were used without further purification. Ultrapure water was taken from a Milli-Q water treatment system (Merck Millipore) and used for all given experiments.

Synthesis: In a typical reaction, 3R-$AgAlO_2$ was prepared by the hydrothermal reaction (1.8 g total mass) of Ag_2O (0.957 g, 4.13 mmol, 1.0 eq, >99 %, Carl Roth, lot: 207258506) and α-Al_2O_3 (0.843 g, 8.26 mmol, 2.0 eq, 99+, 40 nm APS, Chempur, lot: 29092015). The reactants were mixed in an agate mortar and placed in the 45 ml PTFE-lined pressure vessel (Model 4744, Parr Instrument Company), which was then filled with 30 ml of 0.9 M NaOH solution (NaOH: >99 %, Carl Roth, lot: 166238400). The pressure vessel was sealed and heated to the desired reaction temperature of 483 K with a rate of 5 $Kmin^{-1}$. The maximum temperature was held constant for 30 h. After reaching room temperature, the pressure vessel was opened, and the polycrystalline product was recovered by filtration, followed by a deionized water rinse to remove any NaOH traces. The sample was washed several times until the conductivity of the washing medium was below 0.5 $mScm^{-1}$. Afterwards, the sample was dried at 333 K for 12 h. To minimize any photochromic decomposition of the 3R-$AgAlO_2$, the samples were kept away from light.

3R-$AgGaO_2$ and 3R-$AgInO_2$ were prepared in a modified procedure. 3R-$AgGaO_2$ was prepared from Ga_2O_3 (1.11 g, 5.93 mmol, 2.0 eq, 99.999 %, Carl Roth, lot: 465236502) and Ag_2O (0.688 g, 2.97 mmol, 1.0 eq, >99 %, Carl Roth, lot: 207258506) and the hydrothermal synthesis time was reduced to 10 h. In the case of 3R-$AgInO_2$, equimolar ratios of In_2O_3 (0.981 g, 3.53 mmol, 1.0 eq, 99.999 %, Carl Roth, lot: 033195971) and Ag_2O (0.819 g, 3.53 mmol, 1.0 eq, >99 %, Carl Roth, lot: 207258506) were used.

Characterization: Powder X-ray diffraction (PXRD) data was recorded on a STOE STADI P transmission diffractometer using a primary focusing Ge monochromator for Cu $K\alpha_1$ radiation and a DECTRIS MYTHEN 1K position sensitive solid-state detector. The finely ground sample powders were fixed between two layers of thin polyacetate film with small amounts of X-ray amorphous grease before mounting. In addition, PXRD measurements were performed in Bragg-Brentano geometry on a D8 Advance II theta/theta diffractometer (Bruker AXS), using Ni filtered Cu $K\alpha_{1,2}$ radiation and a position sensitive energy dispersive LynxEye silicon strip detector. The sample powder was filled into the recess of a cup-shaped sample holder, the surface of the powder bed being flush with the sample holder edge (front loading). Pattern fitting and phase analysis

were performed by using the Rietveld method as implemented in the TOPAS software package (TOPAS version 5.0, 1999 – 2014 Bruker AXS)

Elemental analysis was performed by inductively coupled plasma atomic emission spectroscopy (ICP-OES). Each sample (58 – 83 mg) was dissolved in a mixture of 100 mg LiF (Merck), 5.0 ml H_2O and 5.0 m HNO_3 (65 %, suprapur,Merck) while heating to 503 K for 2 h using a Multiwavve PRO microwave (Anton Parr). The obtained solutions were diluted to 50 ml with H_2O. From this solution, a 100 µl sample was mixed with 65 µl HNO_3 (65 %, suprapur, Merck) and further diluted to 13 ml with H_2O prior to the analysis. The analysis was performed using an Optima 8300 optical emission spectrometer (Perkin Elmer) in axial mode. For the evaluation, commercial multi-element standards (Certipur,Merck) were used. Data analysis was performed using the Syngistix software for ICP (Perkin Elmer).

The Brunauer–Emmett–Teller (BET) surface area[34] was calculated on basis of N_2 physisorption isotherms which were obtained at liquid nitrogen temperature (77 K) using an Autosorb-6B2-KR (Quantachrome). Prior to measurement, the samples had been degassed at 373 K using an Autosorb Degasser setup (Quantachrome).

UV-vis Diffuse reflectance spectroscopy (UV-Vis DRS) was performed with a Lambda 650 UV Vis spectrometer (Perkin Elmer) equipped with a Praying Mantis™ diffuse reflectance attachment (DRP-SAP, Harrick). Data were recorded in reflectance percentage and afterwards converted to Kubelka-Munk function to determine the optical band gap. A baseline spectrum in the range of 800 – 300 nm of $BaSO_4$ (Merck, Lot: K44813948409) as white standard was collected prior to the experiment. 3R-Ag*B*O_2 (*B*: Ga, In) samples were diluted with $BaSO_4$ prior to the measurement.

Raman measurements were conducted using a confocal microscope system (S&I Spectroscopy & Imaging GmbH) with a monochromator (750 mm focal length, Princeton Instruments) at ambient temperature. Prior to the measurement calibration of the spectrometer frequency was performed by using a Si wafer (520.7±0.5 cm^{-1}). All samples were excited by a 532 nm laser (Samba CW DPSSL, Cobolt) with the laser power lower than 0.5 mW (600 gr/mm, resolution: 1.4 – 1.0 cm^{-1}). Scattered light signals were monitored by a back-illuminated CCD detector (PyLoN:2K, Princeton Instruments).

Conductivity measurements of the powdered samples were performed using the contact free Microwave Cavity perturbation technique (MCPT) in the setup published previously.[35] The measurements were performed at two temperatures, first 473 K and then at 303 K, and with an applied flow of 10 mL/min N_2. The temperature of the cavity used was kept at 293 K. The TM_{010} mode of an S-band resonator (resonance frequency of 3.26 GHz) was used for all measurements. The reflection coefficient was measured in a frequency range of 3.23 to 3.28 GHz while scanning 20001 points using an IFBW of 500 Hz. Three such measurements were averaged to give one data point, which was fit to determine the quality factor using Kajfez' algorithm.[36] Ten data points were averaged to result in average quality factors. From the quality factors of measurements with and without sample, the conductivities were determined, taking into account the crystallographic densities of the compounds to account for the filling fraction of the powders in the MCPT sample holder.

Simultaneous thermal analysis (STA) measurements (TG/DSC) were performed using a STA 449 C Jupiter thermoanalyzer (Netzsch) under a controlled gas atmosphere (Ar, 100 $mlmin^{-1}$). The evolved gases are monitored by a quadrupole mass spectrometer (QMS200 Omnistar, Balzers) coupled to STA via a quartz capillary heated to 313 K. Each measurement was performed with approximately 20 mg sample heating at 5 $Kmin^{-1}$ to 1273 K. Upon cooling to room temperature, the residual powder was further analyzed by XRD analysis. All data were analyzed including TG and DSC curve smoothing using the NETZSCH Proteus Thermal Analysis software package (Version 6.10).

Scanning electron microscopy (SEM) images were taken on a S-4800 SEM (Hitachi) equipped with a field emission gun (FEG) system. The sample was dispersed on a tape of conductive carbon (Plano). The SEM was operated at low accelerating voltage (1.5 kV) for increased resolution of the surface features of the sample. Elemental analysis was performed at elevated accelerating voltages (20 kV) using an energy dispersive X-ray spectroscopy SDD (silicon drift detector, Bruker) connected to the SEM.

For transmission electron microscopy (TEM) analysis the samples were examined in the double Cs corrected microscope under an accelerating voltage of 200 keV (JEM-ARM200F, JEOL). HR STEM images were acquired with spot size 8C, condenser aperture of 30 µm, and camera length of 2 cm. For the imaging a Gatan high-angle annular dark field (HAADF) and an annular bright-field (ABF) detector were used. All 3R-Ag*B*O_2 (*B*: Al, Ga, In) samples were prepared by the standard cross-section method.

X-ray photoelectron spectroscopy (XPS) was measured with a monochromatic Al K_α source (SPECS XR 50) and a hemispherical analyzer (SPECS Phoibos-Has 3500). The pelletized samples were mounted on a sapphire sample holder, between a stainless-steel back-plate and a lid with a 6 mm hole. All XP spectra were collected in normal photoemission mode with E_{pass}= 20 eV. Charging of the samples by 3-6 eV was observe during the acquisition of the spectra. All spectra were aligned using the Fermi edge with an accuracy of 0.1 eV

All density functional theory calculations were performed using the Quantum ESPRESSO package version 6.3[37] using the Perdew Wang LDA[38], Perdew Burke Ernzerhof GGA (PBE)[39], and the Strongly Constrained and Appropriately Normed Semilocal Density Functional (SCAN)[40] functionals as noted in the text. Norm conversing pseudopotentials were employed with a planewave basis set using a kinetic energy cutoff of 120 Ry and a 6x6x1 **k**-point mesh for the crystallographic unit cell; a 12x12x2 mesh was used to generate PDOS plots. The cell shape/volume and ionic positions were optimized for 3R-Ag*B*O_2 (*B*: Al, Ga, In) starting from the published crystal structure of 3R-$AgInO_2$ (ICSD entry 202429[9]). The IR and Raman spectra were calculated at the Γ-point using LDA by way of density functional perturbation theory as implemented in the Phonon package[37].

Acknowledgements

The authors thank J. Allan for XRD and TG/DSC/EG measurements, M. Hashagen and J. Plagemann for N_2 physisorption measurements, W. Frandsen and D. Ivanov for SEM and EDX measurements and Dr. Y. Wang for Raman measurements. We thank Höchstleistungszentrum

Stuttgart (HLRS) for access to the supercomputer HazelHen. This work was conducted in the framework of the BasCat collaboration between BASF SE, TU Berlin, FHI, and the cluster of excellence “Unified Concepts in Catalysis” (UniCat www.unicat.tu-berlin.de).

Conflict of interest

The authors declare no conflict of interest.

Keywords: Ag-delafossite • $AgAlO_2$ • $AgGaO_2$ • $AgInO_2$ • Hydrothermal synthesis

[1] S. Friedel, S. C. R. Acad. Sci. Paris 1873, 77, 211.

[2] a) R. D. Shannon, C. T. Prewitt, D. B. Rogers, Inorg. Chem. 1971, 10, 719-723; b) W. C. Sheets, E. Mugnier, A. Barnabé, T. J. Marks, K. R. Poeppelmeier, Chem. Mat. 2006, 18, 7-20; c) W. C. Sheets, E. S. Stampler, M. I. Bertoni, M. Sasaki, T. J. Marks, T. O. Mason, K. R. Poeppelmeier, Inorg. Chem. 2008, 47, 2696-2705; d) D. Y. Shahriari, N. Erdman, U. T. M. Haug, M. C. Zarzyczny, L. D. Marks, K. R. Poeppelmeier, J. Phys. Chem. Solids 2003, 64, 1437-1441; e) R. Shannon, Acta Cryst. 1976, A32, 751-767.

[3] H. Kawazoe, M. Yasukawa, H. Hyodo, M. Kurita, H. Yanagi, H. Hosono, Nature 1997, 389, 939-942.

[4] a) S. Ouyang, H. Zhang, D. Li, T. Yu, J. Ye, Z. Zou, J. Phys. Chem. B 2006, 110, 11677-11682; b) S. Ouyang, N. Kikugawa, D. Chen, Z. Zou, J. Ye, J. Phys. Chem. C 2009, 113, 1560-1566; c) S. Kumar, H. C. Gupta, Comput. Theor. Chem. 2011, 977, 78-85; d) K. Mukesh, Z. Hanyue, P. Clas, Semicond. Sci. Technol. 2013, 28, 065003; e) H. F. Jiang, C. Y. Gui, Y. Y. Zhu, D. J. Wu, S. P. Sun, C. Xiong, X. B. Zhu, Journal of Alloys and Compounds 2014, 582, 64-68; f) M.-S. Miao, S. Yarbro, P. T. Barton, R. Seshadri, Phys. Rev. B 2014, 89, 045306; g) M. F. Iozzi, P. Vajeeston, R. Vidya, P. Ravindran, H. Fjellvag, RSC Advances 2015, 5, 1366-1377; h) H. C. Kandpal, R. Seshadri, Solid State Sci. 2002, 4, 1045-1052.

[5] a) T. Otabe, K. Ueda, A. Kudoh, H. Hosono, H. Kawazoe, Appl. Phys. Lett. 1998, 72, 1036-1038; b) K. A. Vanaja, R. S. Ajimsha, A. S. Asha, M. K. Jayaraj, Appl. Phys. Lett. 2006, 88, 212103; c) H. Kawazoe, H. Yanagi, K. Ueda, H. Hosono, MRS Bulletin 2011, 25, 28-36.

[6] a) Y. Maruyama, H. Irie, K. Hashimoto, J. Phys. Chem. B 2006, 110, 23274-23278; b) H. Dong, Z. Li, X. Xu, Z. Ding, L. Wu, X. Wang, X. Fu, Appl. Catal., B 2009, 89, 551-556.

[7] B. U. Köhler, M. Jansen, Z. Anorg. Allg. Chem. 1986, 543, 73-80.

[8] M. A. Marquardt, N. A. Ashmore, D. P. Cann, Thin Solid Films 2006, 496, 146-156.

[9] B. U. Köhler, M. Jansen, J. Solid State Chem. 1987, 71, 566-569.

[10] G. Brachtel, M. Jansen, Cryst. Struct. Com. 1981, 10, 173-174.

[11] D. R. Lide, CRC handbook of chemistry and physics : a ready-reference book of chemical and physical data, CRC Press, Boca Raton, Fla., 2009.

[12] R. D. Shannon, D. B. Rogers, C. T. Prewitt, Inorg. Chem. 1971, 10, 713-718.

[13] W. J. Croft, N. C. Tombs, R. E. England, Acta Crystallogr. 1964, 17, 313.

[14] M. Akhtar, M. Menon, M. Sunkara, G. Sumanasekera, A. Durygin, J. B. Jasinski, J. Alloys Compd. 2015, 641, 87-92.

[15] a) W. T. A. Harrison, T. M. Nenoff, T. E. Gier, G. D. Stucky, Inorg. Chem. 1993, 32, 2437-2441; b) P. Halasyamani, M. J. Willis, C. L. Stern, K. R. Poeppelmeier, Inorganica Chim. Acta 1995, 240, 109-115.

[16] D. Xiong, X. Zeng, W. Zhang, H. Wang, X. Zhao, W. Chen, Y.-B. Cheng, Inorganic Chemistry 2014, 53, 4106-4116.

[17] R. Albrecht, Angew. Chem. Int. Ed. Engl. 1985, 24, 1026-1040.

[18] W. L. Suchanek, M. M. Lencka, R. E. Riman, in Aqueous Systems at Elevated Temperatures and Pressures (Eds.: R. Fernández-Prini, A. H. Harvey), Academic Press, London, 2004, pp. 717-744.

[19] W. Gessner, Z. Anorg. Allg. Chem. 1968, 360, 247-258.

[20] D. J. Wesolowski, S. E. Ziemniak, L. M. Anovitz, M. L. Machesky, P. Bénézeth, D. A. Palmer, in Aqueous Systems at Elevated Temperatures and Pressures, Academic Press, London, 2004, pp. 493-595.

[21] R. Gout, G. Verdes, Eur. J. Mineral. 1993, 5, 215-218.

[22] a) D. A. Palmer, P. Bénézeth, D. J. Wesolowski, Geochim. Cosmochim. Acta 2001, 65, 2081-2095; b) P. Bénézeth, D. A. Palmer, D. J. Wesolowski, Geochim. Cosmochim. Acta 2001, 65, 2097-2111.

[23] a) S. Castet, J.-L. Dandurand, J. Schott, R. Gout, Geochim. Cosmochim. Acta 1993, 57, 4869-4884; b) W. L. Bourcier, K. G. Knauss, K. J. Jackson, Geochim. Cosmochim. Acta 1993, 57, 747-762.

[24] a) A. Wichainchai, P. Dordor, J. P. Doumerc, E. Marquestaut, M. Pouchard, P. Hagenmuller, A. Ammar, J. Solid State Chem. 1988, 74, 126-131; b) R. N. Attili, R. N. Saxena, A. W. Carbonari, J. Mestnik Filho, M. Uhrmacher, K. P. Lieb, Physical Review B 1998, 58, 2563-2569.

[25] H. L. Johnston, F. Cuta, A. B. Garrett, J. Am. Chem. Soc. 1933, 55, 2311-2325.

[26] B. G. Pound, D. D. Macdonald, J. W. Tomlinson, Electrochim. Acta 1979, 24, 929-937.

[27] I. I. Diakonov, G. S. Pokrovski, P. Bénézeth, J. Schott, J.-L. Dandurand, J. Escalier, Geochim. Cosmochim. Acta 1997, 61, 1333-1343.

[28] L. C. A. Thompson, R. Pacer, J. Inorg. Nucl. Chem. 1963, 25, 1041-1044.

[29] E. Kroumova, M. I. Aroyo, J. M. Perez-Mato, A. Kirov, C. Capillas, S. Ivantchev, H. Wondratschek, Phase Transitions 2003, 76, 155-170.

[30] R. Nagarajan, N. Tomar, J. Solid State Chem. 2009, 182, 1283-1290.

[31] a) J. Pellicer-Porres, A. Segura, E. Martínez, A. M. Saitta, A. Polian, J. C. Chervin, B. Canny, Phys. Rev. B. 2005, 72, 064301; b) J. Pellicer-Porres, D. Martínez-García, A. Segura, P. Rodríguez-Hernández, A. Muñoz, J. C. Chervin, N. Garro, D. Kim, Phys. Rev. B. 2006, 74,

184301; c) O. Aktas, K. D. Truong, T. Otani, G. Balakrishnan, M. J. Clouter, T. Kimura, G. Quirion, J. Phys. Condens. Matter. 2012, 24, 036003.

[32] a) G. E. Brown, Jr., V. E. Henrich, W. H. Casey, D. L. Clark, C. Eggleston, A. Felmy, D. W. Goodman, M. Gratzel, G. Maciel, M. I. McCarthy, K. H. Nealson, D. A. Sverjensky, M. F. Toney, J. M. Zachara, Chem Rev 1999, 99, 77-174; b) H. Knözinger, P. Ratnasamy, Catal. Rev. 1978, 17, 31-70.

[33] W. M. Haynes, CRC Handbook of Chemistry and Physics, 96 th ed., CRC Press, 2015.

[34] S. Brunauer, P. H. Emmett, E. Teller, J. Am. Chem. Soc. 1938, 60, 309-319.

[35] M. Eichelbaum, R. Stößer, A. Karpov, C.-K. Dobner, F. Rosowski, A. Trunschke, R. Schlögl, Phys. Chem. Chem. Phys. 2012, 14, 1302-1312.

[36] D. Kajfez, Q factor measurements using MATLAB, Artech House, Norwood, 2011.

[37] a) G. Paolo, B. Stefano, B. Nicola, C. Matteo, C. Roberto, C. Carlo, C. Davide, L. C. Guido, C. Matteo, D. Ismaila, C. Andrea Dal, G. Stefano de, F. Stefano, F. Guido, G. Ralph, G. Uwe, G. Christos, K. Anton, L. Michele, M.-S. Layla, M. Nicola, M. Francesco, M. Riccardo, P. Stefano, P. Alfredo, P. Lorenzo, S. Carlo, S. Sandro, S. Gabriele, P. S. Ari, S. Alexander, U. Paolo, M. W. Renata, J. Phys. Condens. Matter. 2009, 21, 395502; b) P. Giannozzi, O. Andreussi, T. Brumme, O. Bunau, M. B. Nardelli, M. Calandra, R. Car, C. Cavazzoni, D. Ceresoli, M. Cococcioni, N. Colonna, I. Carnimeo, A. D. Corso, S. d. Gironcoli, P. Delugas, J. R. A. DiStasio, A. Ferretti, A. Floris, G. Fratesi, G. Fugallo, R. Gebauer, U. Gerstmann, F. Giustino, T. Gorni, J. Jia, M. Kawamura, H. Y. Ko, A. Kokalj, E. Küçükbenli, M. Lazzeri, M. Marsili, N. Marzari, F. Mauri, N. L. Nguyen, H. V. Nguyen, A. Otero-de-la-Roza, L. Paulatto, S. Poncé, D. Rocca, R. Sabatini, B. Santra, M. Schlipf, A. P. Seitsonen, A. Smogunov, I. Timrov, T. Thonhauser, P. Umari, N. Vast, X. Wu, S. Baroni, J. Phys. Condens. Matter. 2017, 29, 465901.

[38] J. P. Perdew, Y. Wang, Phys. Rev. B 1992, 45, 13244-13249.

[39] J. P. Perdew, K. Burke, M. Ernzerhof, Phys. Rev. Lett. 1996, 77, 3865-3868.

[40] J. Sun, A. Ruzsinszky, J. P. Perdew, Phys. Rev. Lett. 2015, 115, 036402.